NUMERICAL ANALYSIS OF THE FLOW DYNAMICS OF AN N_2 CRYOGENIC JET

by

Chafik BENSALEM[a], Abdallah BENAROUS[b*], and Pierre-Olivier LOGERAIS[c]

[a] LCEMSM Laboratory, Mechanical Engineering Department, Faculty of Technology, Hassiba Benbouali University of Chlef, Chlef, Algeria
[b] Faculty of Technology, University of Blida 1, Blida, Algeria
[c] Universite Paris-Est, CERTES, IUT de Senart-Fontainebleau, Lieusaint, France

Original scientific paper
https://doi.org/10.2298/TSCI190805162B

Injection and mixing of cryogenic propellants are very complex at near-critical and supercritical conditions. The concise description and the reliable measurements on such flows are still questionable. In this work, a RANS study is performed for a pure N_2 fluid injection at transcritical conditions on a laboratory scale test rig. An in-depth thermodynamical analysis on the real-gas behavior has allowed N_2 density prediction over the experimental range of the injection temperature and for several equations of state. A focus was thrown on the prediction of the density evolution on the chamber centerline and across the injector. The calculations were performed using both adiabatic and constant temperature conditions for the injector wall. The inner heat transfer in the injector had a significant effect on the jet density distribution and therefore, on the overall flow dynamics. Numerical results regarding axial profiles of density and dense core lengths agree fairly well with the experimental data provided by the literature.

Introduction

Liquid rocket engines (LRE) have imposed their utilization among several chemical propulsive systems for space conquest missions. The LRE are still considered as the most reliable and controllable devices for satellite launchers [1].

According to storage conditions, liquid propellants that feature propulsive chambers in LRE are classified into storable (ambient-T) and cryogenic (low-T) couples. Cryogenic reactants are almost generalized for injection devices including launchers and main engines of shuttles as well as laboratory scale benches owing to several criteria related to thrusts and overall masses of launchers [2]. Indeed, liquid oxygen (LOX) associated to gaseous hydrogen (GH_2) or LOX/CH_4 propellants offer a high specific impulse, short kinetic times and wide ranges of flammability, allowing for safe combustion in extreme conditions [3].

The injection head consisting of hundreds of individual injector elements is the most important sub-device of LRE for such combinations. The injection configuration (shear, swirl, and impingement) influences on the overall performances of the engines while heat transfer within the injector elements is strongly linked to the chamber wall durability and to the combustion instability [4].

* Corresponding author, e-mail: abenarous@yahoo.fr

The physical and dynamical problems related to the injection of propellants are very complex, exhibiting flame-acoustic coupling and 3-D flow patterns involving interaction of the multiple injectors [5]. As numerical models could not reproduce all the complexities, research facilities feature uni-element injection with appropriate mixture ratios and flow rates of propellants to mimic as close as possible the operating conditions of rocket engines.

Pure-fluid conditions of injections could be at sub, trans or supercritical thermodynamic states under various flow rates for these combustion facilities. Hence, the propellant mixture showcases critical mixing lines instead of just one critical point whereas several thermodynamical regimes involving ligaments, droplets or even supercritical fluids can take place simultaneously [6].

Consequently, thermodynamic and transport properties of the mixture may be strongly affected by minor changes in temperature while the flow exhibits huge gradients in density which obviously affect the density-weighted (Favre averaged) variables. Moreover, the molecular interaction leads to significant deviations from the ideal-gas behavior and the thermodynamic descriptions need to account for the properties of the real gas states [7]. This characteristic is more pronounced in cold-flow conditions, where the turbulent mixing between propellants is made prior to ignition.

Distinct series of experimental investigations have been conducted on research-test facilities under different chamber pressures and for several combinations of propellants to obtain the information on flow phenomena near the injector. Experimental investigations concerning the cryogenic combustion of LOX/GH_2 have been reported in several works [8-10] on the German Aerospace Centre rig where authors largely studied spray and injection phenomena in cryogenic rocket engines. Candel *et al.* [11] inquired on the reactive case of high pressure shear coaxial injector flame in the ONERA test rig and highlighted the importance of the injection conditions in the flame attachment process. Several experimental and numerical investigations focused on transcritical and supercritical injection using a pure inert fluid owing to a strong physical coupling between injection propellants, heat exchanges and thermodynamics.

In this direction, some experimental works have been realized on cryogenic nitrogen into a supercritical nitrogen environment [9, 12-14]. The major finding of these studies was the strong influence of the thermodynamic state, in particular the jet temperature history, on the jet development downstream the injector exit. In this context, Mayer [12] confirmed that small shifts in N_2 jet temperature induce much higher changes in density. The authors related the N_2 temperature fluctuation the heat transfer for the injector wall. Besides, Branam and Mayer [15] found that the heat transfer from the injector wall to the fluid prior to injection has a strong effect on the turbulence intensity within the mixing zone and thereby on the overall jet flow evolution.

The aforementioned experimental campaigns were completed by several numerical studies on trans and supercritical injection, including real gas effects. Non-reactive calculations using large-eddy simulation (LES) were early attributed to Oefelein [16], Hosangadi *et al.* [17] and Schmitt *et al.* [18]. These investigations have revealed the significance of accounting for the thermodynamic non-idealities in view of achieving accurate results. Specific attention was paid to mixing layer stability of non-reactive pure fluids on coaxial injection configurations. The RANS simulations have been widely employed for turbulent mixing description and flame structure characterization on the grounds of their low computational cost. Several authors have succeeded in reproducing the mean flow properties in both non-reactive and reactive conditions [19-23]. In LOX/GH_2 supercritical conditions, Benarous and Liazid [24] used a real-gas mixing-law for density, with enhanced transport properties to obtain the mean flame length and the OH mass fraction which were fairly close to the ONERA experiments. In the same directi-

on, Benmansour *et al.* [23] performed a 3-D-RANS simulation on the A60 point Mascotte-rig, with piecewise polynomial expressions for the LOX and the GH_2 densities, as provided from the NIST database. These authors have recovered a density fluctuation near the injector exit, which was close to ONERA measurements.

A complex configuration featuring injection, mixing and combustion at trans or supercritical condition was investigated in the work of Kim *et al.* [25]. The authors stated out a meaningful discrepancy between the real-gas and the ideal-gas density for both the near-injector and the chamber-axis regions.

Some works have been devoted to predict the density evolution for various equations of state (EoS). The most popular descriptions were based on thermodynamic Soave-Redlich-Kwong (SRK) and Peng-Robinson (PR) EoS [26]. At fully supercritical conditions, SRK was considered as the most accurate EoS while in contrast the PR equation revealed a prominent overestimation of the density, specifically in the near-injector region by reason of the under prediction of the boiling temperature [27]. Here several studies concluded that no CFD computations were successful in foreseeing accurately the subsided dense core [20, 21, 23].

Emphasize should be laid on the fact that most of the numerical investigations have considered the adiabatic condition for both the injector and the chamber walls. A strong dependence of the turbulence intensity on heat exchanges between the working fluid and the injector wall have been pointed out by LES simulations of the nitrogen injection in the same context [28]. As per the authors' inference, some reflections are still underway on the injector heat addition modeling and on its influence on the evolution of the dense core. Otherwise, the experimental investigations regarding cryogenic injection have shed into light the relevance of accounting for the heat transfer from the injector wall to the fluid-flow [12].

An attempt towards a numerical characterization of a real-gas N_2 fluid-flow within an injector-chamber assembly injected under trans to super-critical conditions is undertaken in the present framework. A special attention is paid to the density-considered as a yardstick quantity – evolution in the vicinity of the injector exit and on the chamber centerline. Both adiabatic and isothermal injector conditions are considered for the RANS-based calculations. Numerical results regarding spatial distribution of density and dense core length are confronted to the measurements (Case No. 3) of Mayer *et al.* [12], and compared with some empirical values given by widely-used correlations.

Physics description and modeling

Injection and mixing of cryogenic propellants occur specifically under high pressure and low temperature conditions. Consequently, ideal-gas assumption cannot be applied for thermodynamic description of pure species or fuel/oxidizer mixture. Hence, density is derived from an EoS and flow dynamics is strongly related to mass-weighted (Favre) variables.

Thermodynamic modeling

Cubic EoS of the real gas type enable to link the static pressure and the static temperature to the molar volume via an algebraic relation for pure species. The three EoS used are briefly described.

In the SRK EoS, a modification in the basic equation developed by Redlich and Kwong in 1949 is made through the $a(T)$ parameter [29]:

$$P = \frac{\mathrm{R}T}{\upsilon - b} - \frac{a(T)}{\mathrm{v}^2 + \upsilon b} \tag{1}$$

with

$$a(T) = a_0\alpha,\ \alpha = \left[1+\gamma\left(1-\sqrt{T/T_{cr}}\right)\right]^2,\ \gamma = 0.480+1.574\omega-0.176\omega^2$$
$$a_0 = 0.42747\mathrm{R}^2T_{cr}^2/P_{cr},\ b = 0.08664\mathrm{R}T_{cr}/P_{cr}$$

The EoS of PR is very similar to the SRK one, the adjustment is related to the attraction term [30]:

$$P = \frac{\mathrm{R}T}{\upsilon-b}-\frac{a(T)}{\mathrm{v}^2+2\upsilon b-b^2} \tag{2}$$

with

$$a(T) = a_0\alpha,\ \alpha = \left[1+\gamma\left(1-\sqrt{T/T_{cr}}\right)\right]^2,\ \gamma = 0.37464+1.54226\omega-0.26992\omega^2$$
$$a_0 = 0.45724\mathrm{R}^2T_{cr}^2/P_{cr},\ b = 0.07780\mathrm{R}T_{cr}/P_{cr}$$

Concerning Aungier-Redlich-Kwong (ARK) EoS, a change is effected by adding a parameter c and an exponent n to the reduced temperature which is a function of the acentric factor of the pure species [31]:

$$P = \frac{\mathrm{R}T}{\upsilon-b+c}-\frac{a(T)}{\mathrm{v}^2+\upsilon b} \tag{3}$$

with

$$a(T) = a_0(T/T_{cr})^{-n},\ n = 0.4986+1.1735\omega+0.4754\omega^2,\ a_0 = 0.42747\mathrm{R}^2T_{cr}^2/P_{cr},$$
$$b = 0.08664\mathrm{R}T_{cr}/P_{cr},\ c = \frac{\mathrm{R}T_{cr}}{P_{cr}+a_0/(V_{cr}^2+V_{cr}b)}+b-V_{cr}$$

In the aforementioned formulation, $P_{cr} = 33.9$ bar, $T_{cr} = 126.2$ K, $V_{cr} = 3.2\cdot10^{-3}$ m^3/kg, and $\omega = 0.037$ correspond successively to the critical pressure, the critical temperature, the critical volume and the acentric factor of the N_2, γ, and n are functions of the acentric factor, $a(T)$ and b are parameters that in turn account for the attraction forces and the proper volume of molecules.

Flow dynamics modelling

The stationary reacting flow equations of mass, momentum, and specific energy are expressed in conservative forms:

$$\vec{\nabla}(\rho\vec{\mathrm{u}}) = 0 \tag{4}$$

$$\rho\vec{\mathrm{u}}\left(\vec{\nabla}\vec{\mathrm{u}}\right) = -\vec{\nabla}p+\vec{\nabla}\boldsymbol{\tau} \tag{5}$$

where

$$\boldsymbol{\tau} = -\frac{2}{3}\mu\left(\vec{\nabla}\vec{\mathrm{u}}\right)\boldsymbol{I}+\mu\left(\vec{\nabla}\vec{\mathrm{u}}+\vec{\nabla}\vec{\mathrm{q}}\right) \tag{6}$$

The $\boldsymbol{\tau}$ and $\boldsymbol{I}$ are the viscous stress and the identity tensors, respectively, and μ is the molecular dynamic viscosity:

$$\rho\vec{\mathrm{u}}\vec{\nabla}e = -p\vec{\nabla}\vec{\mathrm{u}}+\tau\vec{\nabla}\vec{\mathrm{u}}-\vec{\nabla}\vec{\mathrm{q}} \tag{7}$$

where e and q are the specific internal energy and the total heat fluxes, respectively. By neglecting the molecular diffusion caused by temperature gradient (Soret effect) and the thermal diffusion engendered by a concentration gradient (Dufour effect), the heat flux can be given:

$$\vec{\mathrm{q}} = -\lambda\vec{\nabla}T + \Sigma_\alpha \rho D_\alpha h_\alpha \nabla Y_\alpha \tag{8}$$

where

$$h_\alpha = \int_{T^0}^{T} c_{p\alpha}\mathrm{d}T + h_{\alpha,F} \tag{9}$$

is the partial enthalpy of the i^{th} species in the mixture.

Solving the previous system of equations in a direct manner is not feasible for most turbulent flow calculations. Averaged forms are mandatory to access the mean quantities of the flow unknowns. Every extensive quantity φ (except density and pressure), can be decomposed into a mean part $\tilde{\varphi}$ and a fluctuating par φ'':

$$\varphi = \tilde{\varphi} + \varphi'' \tag{10}$$

where the Favre (mass weighted) averaging form is defined

$$\tilde{\varphi} = \frac{\overline{\partial\varphi}}{\overline{\rho}} \tag{11}$$

The averaging leads to unclosed terms in the momentum and energy equations, which are modeled by using the eddy viscosity and diffusivity hypothesis:

$$-\rho\overline{u_i''u_j''} = \mu\left(\frac{\partial\tilde{u}_i}{\partial x_j} + \frac{\partial\tilde{u}_j}{\partial x_i} - \frac{2\delta_{ij}}{3}\frac{\partial\tilde{u}_k}{\partial x_k}\right)_t \tag{12}$$

$$-\rho\overline{u_j''h''} = \frac{\mu_t}{\mathrm{Pr}_t}\frac{\partial\tilde{h}}{\partial x_j} \tag{13}$$

where Pr_t is the turbulent Prandtl number, set to its default value $\mathrm{Pr}_t = 0.7$. The system of equations can be closed by choosing a model for the turbulent viscosity μ_t. In this work, this is done by a standard k-ε turbulence model, by solving two additional transport equations for the turbulent kinetic energy k and its dissipation rate ε. The turbulent viscosity is modeled [32]:

$$\mu_t = \frac{C_\mu\overline{\rho}\tilde{k}^2}{\tilde{\varepsilon}} \tag{14}$$

It is well known that the standard k-ε model was initially developed for plane jets and overestimates mixing and turbulence levels of axisymmetrical jets [33]. Thereupon, a slight modification of the standard k-ε model is proposed. Hence, a Pope correction term is added to the kinetic energy dissipation rate equation [34]. This modification is done by supplementing a production term which accounts for the vortex stretching effect on the jet viscosity and in so doing on its spreading rate:

$$\frac{\partial}{\partial x_j}\left(\overline{\rho}\tilde{u}_j\tilde{\varepsilon}\right) = \frac{\partial}{\partial x_j}\left(\frac{\mu_t}{\sigma_\varepsilon}\frac{\partial\tilde{\varepsilon}}{\partial x_j}\right) + \frac{\tilde{\varepsilon}}{\tilde{k}}\left(C_{1\varepsilon}P_K - \overline{\rho}C'_{2\varepsilon}\tilde{\varepsilon}\right) \tag{15}$$

where

$$P_K = -\overline{\rho u_i''u_j''}\frac{\partial\tilde{u}_i}{\partial x_j} \tag{16}$$

stands for the production rate of the turbulence energy and $\chi = \omega_{ij}\omega_{jk}S_{ki}$ with:

$$\omega_{ij} = \frac{1}{2}\frac{\tilde{k}}{\tilde{\varepsilon}}\left[\frac{\partial \tilde{u}_i}{\partial x_j} - \frac{\partial \tilde{u}_j}{\partial x_i}\right],\ S_{ij} = \frac{1}{2}\frac{\tilde{k}}{\tilde{\varepsilon}}\left[\frac{\partial \tilde{u}_i}{\partial x_j} + \frac{\partial \tilde{u}_j}{\partial x_i}\right] \tag{17}$$

Here χ is the invariant vortex stretching and $C_{3\varepsilon}$ is a strictly positive Pope constant. The correction is done by choosing an appropriate value for the new turbulence constant appearing in eq. (15):

$$C'_{2\varepsilon} = C_{2\varepsilon} - \chi C_{3\varepsilon} \tag{18}$$

The length of the dense core (X_c/d) is the distance at which the centerline density stays relatively constant. Harsha [35] provided an empirical approximation for this quantity based on the injector Reynolds number and validated it for fully developed low density flows:

$$\text{——} \quad 2.13\,\mathrm{Re}^{0.097} \tag{19}$$

Furthermore, Chehroudi *et al.* [36] developed an empirical formulation for the dense core based on the ratio $\rho_0/\rho_\infty\,\rho$ adapted for high density flows:

$$\frac{X_C}{d} = C\left(\frac{\rho_0}{\rho_\infty}\right)^{1/2} \tag{20}$$

where $11 \geq C \geq 3.3$ stands for an empirical constant of the model.

A more developed empirical relation accounting for high densities and validated against experimental data over several ranges of pressure, temperature and velocity, was suggested by [12]:

$$\frac{X_C}{d} = 3.344\cdot 10^{-5}\,\mathrm{Re}_\infty^{0.5597}\left(\frac{\rho_\infty}{\rho_0}\right)^{-3.179}\gamma^{-0.9934}\times\left(\frac{T_0}{T_{\mathrm{cr}}}\right)^{5.987}\left(\frac{P_0}{P_{\mathrm{cr}}}\right)^{-0.5043} + 7.363 \tag{21}$$

Test rig description and operating conditions

The experiments of Mayer *et al.* [12] investigate the behavior of a cryogenic, axisymmetric N_2 jet in transcritical conditions. The authors carried out several tests under fully-supercritical conditions where the chamber pressure reached 5.96 MPa for a maximum N_2 injection temperature of 130 K. Despite the abundant data of measurements, the Raman-based records for temperature of the N_2 jet at the injector exit disclose high dispersions [15].

The test rig consists of a cylindrical injector having a diameter of 2.2 mm and a length of 90 mm. The length-to-diameter ratio is over 40 which is expected to yield a fully developed pipe flow at the injector exit section [12]. The chamber is a circular cylinder with a diameter of 122 mm and a length of 1 m equipped with an electrical heater to keep the chamber wall temperature at 298 K. The operating conditions with the scalar measurements for the RCM1-A case are recalled in tab. 1.

Table 1. Operating conditions (scalar measurements) for the RCM1-A case [12]

Injector flow characteristics	Values
Chamber pressure [MPa]	3.97
Averaged exit velocity [ms^{-1}]	4.90
Inlet temperature [K] [17]	120.9
Exit temperature [K]	126.9

Results and discussion

Thermodynamic analysis

As the investigated operating point (RCM1-A) is at nearly-critical conditions, it is to be expected that slight temperature deviations may lead to huge density gradients. This way, the

set of EoS described in section *Thermodynamic modeling*, were reformulated into cubic forms $\rho = \rho(P, T)$ using a MATLAB routine [37]. As set out in each equation of state, N_2 density was calculated over a range 120-150 K and confronted with the NIST curve, as well as with perfect-gas values, fig. 1(a).

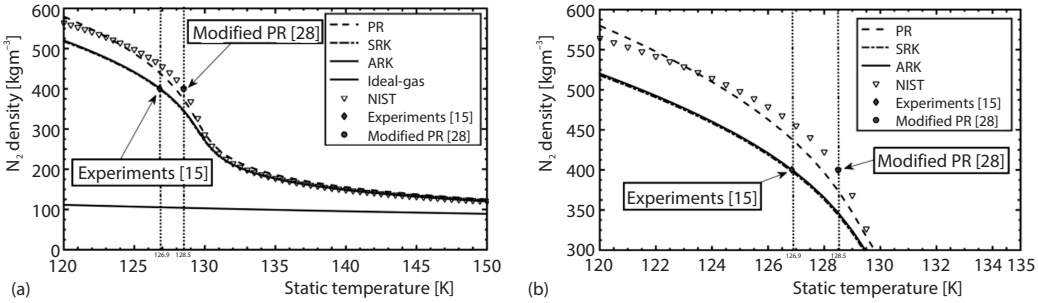

Figure 1. (a) Nitrogen density as a function of static temperature (P = 3.97 MPa) and (b) zoom on the injection area temperature range

Figure 1(a) illustrates that the perfect-gas EoS exhibits a major underestimation of the N_2 density, particularly in the range [120-130 K]. The relative deviation between the ARK/SRK EoS and the perfect-gas prediction is close to 74%, whilst the discrepancy decreases down to 24% at T = 150 K. Thenceforth, the fact of considering the N_2 jet as a perfect gas may lead to tremendous errors on thermodynamic properties, within the cold regions of the flow.

A modified-PR equation of state has been derived by Muller *et al.* [28] with the goal of predicting N_2-density at the injector exit using LES. The authors succeeded in recovering the density value $\rho^* = 400$ kg/m^3 as measured by Branam and Mayer [15] at a slightly high temperature T = 128.5 K, fig. 1(b).

It is to be noted that the N_2 density previewed by the PR equation fits quite well the NIST curve with a global underestimation of 4.8% when above the temperature T = 126.9 K, fig. 1(a). Within the temperature range [120-126.9 K], the nitrogen density achieved by ARK and SRK Eos seems somewhat lower than the NIST-based values.

Nevertheless, the experimental density value ρ^* as recorded at T = 126.9 K is well recovered, using SRK or ARK EoS, fig. 1(b). Beyond the value T = 130 K, PR, ARK, and SRK equations reproduce almost the same N_2 density values.

Numerical analysis

A so-called RCM1 case was defined in the Rocket Combustion Modelling Workshop (IWRCM), as the configuration describes the injection in a cylindrical chamber [38]. The case data aim to mimic the experimental conditions covered by Mayer [12] in campaigns 3 and 11. Here, the considered geometry was comparable to the M51 chamber, featuring a cylindrical part with a diameter of 122 mm and a length of 1000 mm, fig. 2(a), and likewise a duct part (injector) with an inner diameter of 2.2 mm and a length of 90 mm, fig. 2(b). Accordingly, an axisymmetric representation of the domain was adopted for the numerical computations.

As commonly used by the numerical community, the faceplate and the injector walls were considered as adiabatic, while an isothermal condition was set for the chamber walls [38]. The Favre averaged forms of the governing equations were discretized in a finite-volume formulation and numerically resolved by using the commercial package ANSYS-FLUENT [39].

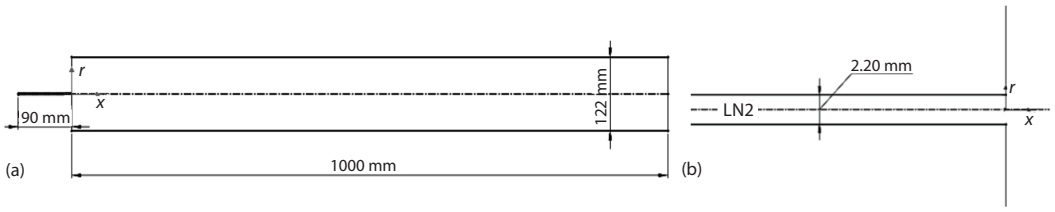

Figure 2. (a) Computational domain geometry and (b) injector model overview

Continuity, momentum, turbulence and energy equations were discretized for the numerical resolution with a first-order upwind scheme and a SIMPLE algorithm for pressure-velocity coupling. Target errors were set to 10^{-4} for all the unknowns except for temperature where a threshold of 10^{-6} was imposed.

The computational domain was covered by a structural grid. A local refinement was operated in the axial direction downstream the injector exit, fig. 3(a). Several grids were used to check the density distribution along the chamber axis, fig. 3(b), over which a fairly good agreement was noticed between the measurements and the numerical values for a mesh of 209160 cells. The latter grid has been retained for the numerical calculations. The coarsened, the retained (baseline) and the refined grids comprise successively 167750, 209160, and 285440 cells, where the injector was resolved with 230×25, 245×28, and 270×36 cells while 720×225, 850×238, and 1025×269 cells were used for the chamber.

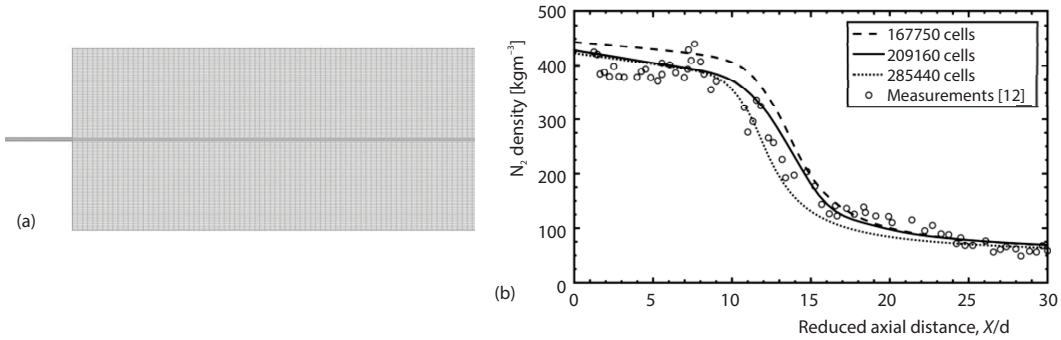

Figure 3. (a) Mesh of the computational domain and (b) grid sensitivity analysis for the centerline density

Prior to flow analysis in the combustion chamber, the jet history within the injector was analyzed. Here, one seeks to recover the appropriate velocity profile and jet temperature at the injector exit section, as indicated in the measurements, tab. 1. In this preliminary investigation, the injector wall was assumed to be isothermal and equal to the chamber-wall temperature $T_{\text{ch-wall}} = T_{\text{inj\_wall}} = 298$ K, so that heat transfer towards the N_2 flow will be considered. As proposed by Cheng and Farmer [40], the inlet turbulent kinetic energy k was quadratically related to the injector inlet velocity by contrast with its dissipation rate ε which was estimated by using the injecor diameter, as a turbulent length scale.

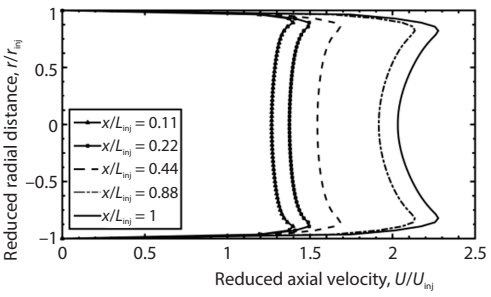

Figure 4. Axial velocity distribution along the injector

Here, several axial stations were considered, fig. 4, and the near-wall velocity of the N_2-flow seems important compared with the centerline values. This reveals a flow acceleration owing to low density values in the injector-wall vicinity, and this is more pronounced in the downstream of $x/L_{inj} = 0.88$ and $x/L_{inj} = 1$.

Although the velocity was not fully developed at the exit section of the injector, the mean experimental value of 4.90 m/s, tab. 1, was numericaly recovered.

Figure 5 shows the axial distribution of N_2 density as obtained numerically by using PR, SRK, and ARK EoS. The numerical density values downstream the injector exit are confronted to the Raman measurements of Mayer [12].

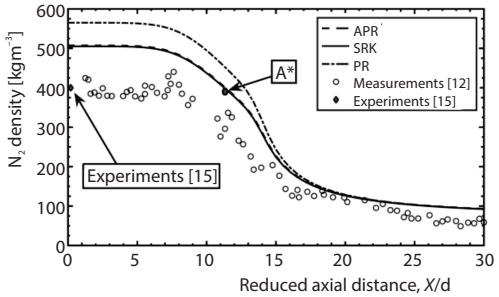

Figure 5. Centerline density distribution (adiabatic case, T_{inlet}=120.9 K, P = 3.97 MPa)

As mentioned in the thermodynamic section, the measurements of Branam and Mayer [15] at the injector exit section provide the value of $\rho^* = 400$ kg/m^3. It should be noted that the PR curve exhibits a relative overestimation close to 42% on the N_2 density, compared with the experimental value ρ^* at the injector exit. More so too, both ARK and SRK EoS predict a slight lower density value at the injector exit, corresponding to a relative deviation of 27%. The ARK curve reaches the experimental value ρ^* not at the injector exit section but far downstream at $X/d = 11.2$ (A*, fig. 5). In this adiabatic study case, the numerical centerline static temperature was close to $T^* = 126.9$ K at the axial location $X/d = 11.2$ as referred to in the thermodynamic section.

With the ARK equation of state, the calculations predict an almost constant density value of $\rho = 507$ kg/m^3 over a distance $X/d \leq 6.1$, fig. 5. In this dense core region, the relative discrepancy between the numerical N_2 density values and the measurements of Mayer [12] ranges from 27-36%. The global deviation tends to decrease by 20% ($\rho = 92$ kg/m^3) downstream the axial location $X/d = 18$, where an asymptotic-like behavior is acquired anew.

The lack of data relative to T and ρ at the injector inlet led some authors to focus their measurements on the N_2 density ρ^* at the injector exit. Since numerical simulations require temperature at the injector inlet section, several models from the literature have been suggested to amend the prescribed test temperature $T_{inlet} = 120.9$ K, see tab. 1, to a slightly elevated value, by reason find back the value of ρ^* at the injector exit section [18, 28, 40].

Accordingly, the adopted adiabatic condition on the injector wall directly implies an isothermal inflow which results in the same temperature on both the injector inlet and outlet. In so doing, the inlet temperature value $T_{inlet} = 126.9$ K has been proposed in the workshop on rocket combustion modelling (IWRCM) [38]. It is worth noticing that the thermodynamic analysis (section *Results and discussion*) employing ARK as an equation of state, has rendered the target density value ($\rho^* = 400$ kg/m^3) at the same temperature $T = 126.9$ K, see fig. 1(a).

The authors of the present work believe that the fact of neglecting the heat transfer from the injector walls to its inflow may mitigate the thermal expansion, thereby inducing high N_2 density values at the injector exit. And more so, the proposed temperature at the injector inlet $T_{inlet} = 126.9$ K fits well the density target value, ρ^*. The latter inlet condition assumes a constant temperature of the injected fluid across the injector. As a result, the test operating point may thus not be fully complied with as prescribed by Mayer [12].

The following calculations use a prescribed constant temperature condition on the injector wall, rather than an adiabatic one. As clearly stated out in the experimental investigation

of Mayer [12], heat transfer in the injector tube is significant, particularly in the warmer cases. Thereafter, it seems reasonable to perform computations taking into account heat transfer from a warm injector wall maintained at ambient temperature $T_{\text{inj\_wall}} = 298$ K to the fluid inside the injector.

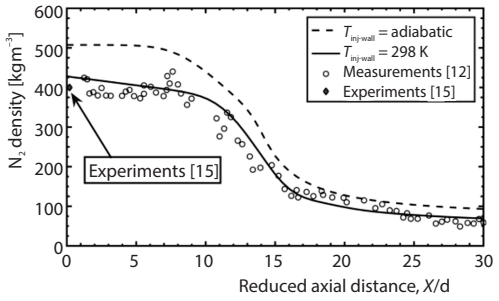

Figure 6. Centerline density distribution (T_{inlet} = 120.9 K, P = 3.97 MPa)

Figure 6 displays the centerline distribution of the N_2 density downstream the injector exit section. Both the adiabatic and the constant temperature conditions on the injector wall are discussed. It is observed that for an isothermal condition, the target density value ρ^* is overestimated by only 7% at the injection exit section. The corresponding density features a linear profile up to X/d = 10 succeeded by a strong slope downfall, which underlines a fast thermal flow expansion in the chamber. Globally, the curve is in keeping with the measurements with an overall relative deviation below 8%.

The obtained density drop-off without a clear dense core can be visualized on the first part of the isothermal curve, fig. 6. This behavior had been numerically acquired by Banuti and Hannemann [41].

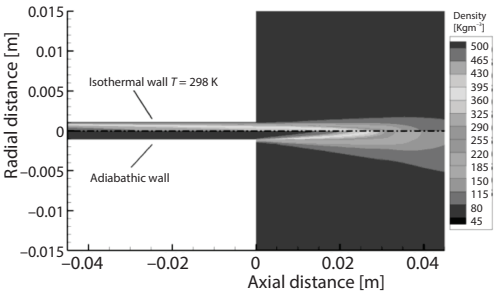

Figure 7. Density contours for the isothermal case (top) and for the adiabatic one (bottom)

As heat transfer inside the injector affects both the axial and the radial distribution of the N_2 density, it appears relevant to present the spatial distribution of the density for both the adiabatic and the isothermal injector. Figure 7 illustrates the contour of the N_2 density within the injector-chamber assembly. For clarity purposes, the contour focuses on one-half of the length of the injector and on 4.5% of the chamber length.

It is clearly displayed that a boundary-layer builds up prior to injection for the isothermal case. Starting from the walls and progressing towards the centerline, the density of N_2 is diminished. The adiabatic dense core reaches $X \sim 0.020$ m and terminates at $X \sim -0.021$ m before entering the chamber in the isothermal case.

As the dense core is at the axial location where the centerline density begins to drop off, a threshold of 10% on the density from the injector outlet can be proposed. Comparative values for dense core lengths given by the three empirical approximations, eqs. (19)-(21), and the values corresponding to the numerical threshold are depicted in fig. 8.

For the adiabatic case, fig. 8 (a), the numerical value for the dense core ($X/d \sim 9.3$) is in accordance with the empirical prediction of Mayer [12] with a relative deviation under 0.5%, but underestimates (~ –5%) the value provided by Chehroudi *et al.* [36].

Despite the minor decrease of the centerline density across the isothermal injector, fig. 7, the chamber downstream the injector exit still contains a dense flow, fig. 6. In this case, the dense core length as supplied by Mayer [12] is overestimated by only 0.23%, fig. 8(b). In addition, a good agreement (~ –1.1%) with the empirical value of Chehroudi *et al.* [36] is achieved.

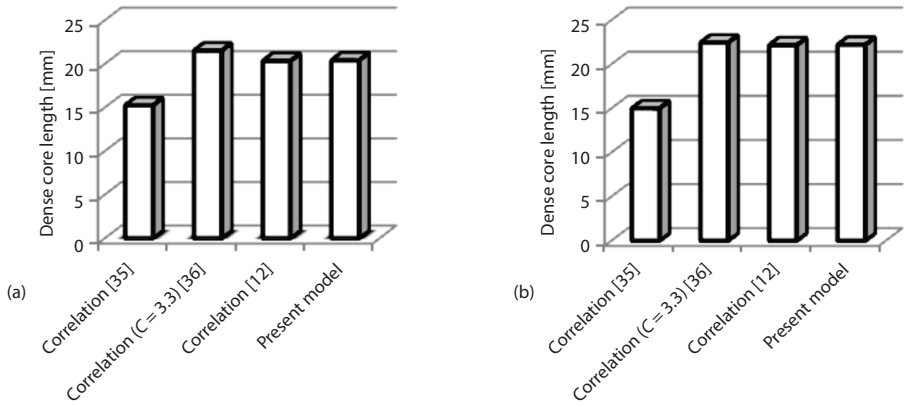

Figure 8. Dense core length comparison for the isothermal injector case

All in all, the threshold proposed for the numerical centerline density appears suitable for both the isothermal and adiabatic injector cases. Indeed, the consistency of the obtained numerical values on dense core length predictions from widely used correlations quantitatively offers a substantial validation

Future advanced CFD computations and concise experimental investigations on both trans- and supercritical injections are still needed for the broader understanding of the dense flow behavior. Additionally on the basis of the dense-core correlations, future work can deal with algebraic calculationols to predict the propellant mixture quality which is intimately related to the efficiency of combustion, without resorting to CFD computations.

Conclusions

A better insight of the modelling requirements for cryogenic injection at trans and supercritical conditions is reached by means of consistent simulations. Cold nitrogen was injected into a chamber at ambient temperature. Several EoS have been used for this real gas application. On the basis of the thermodynamic analysis, the ARK and SRK EoS have allowed a better prediction of the target density value, ρ^*, as provided by the experiments of Mayer [12] whereas the PR EoS overestimated this value by 10%.

A RANS calculation was performed for the realistic test case (case No. 3) of Mayer [12] in the light of the thermodynamical statements. Firstly, the commonly used adiabatic boundary condition for the injector wall was considered in the numerical calculation. The centerline density distribution exhibited a relative difference up to 36% compared to the experiments.

An isothermal injector calculation was hence adopted to account for the heat transfer from the wall to the fluid inside the injector. In this case, the density curve along the chamber axis revealed a good agreement with the experiments, recovering therefore, the far-field density value (ρ_∞= 45 kg/m^3). The comparison of the contours of the density across the injector length and downstream within the chamber region, threw into evidence that the dense core ends before entering the chamber in the isothermal injector whilst it reaches the axial location X/d = 9.1 downstream the injector exit in the adiabatic case. Downstream the injector exit, a criteria based on a relative threshold of 10% for the centerline density was proposed. Accordingly, the calculated dense core values for both the adiabatic and isothermal injector cases are quite near to those provided by the empirical models of Mayer [12] and Chehroudi *et al.* [36].

On the light of the obtained results, the inner heat transfer in the injector seems to have a significant effect on the jet density distribution and therefore, on the overall flow dynamics. The cooling techniques of the injection heads must consider the effect of internal heat input on the liquid propellant density and also on the mixing ratio at the inlet of combustion chamber.

Acknowledgment

The authors would like to thank the DGRSDT entity for the support of this ongoing work under the project No. A11N01UN020120150001.

Nomenclature

a_0 – constants of EoS, [Pam^{-6}mol^{-2}]
c – constants of EoS, [m^{3}mol^{-1}]
c_p – specific heat at constant pressure, [JkgK^{-1}]
$C_{1\varepsilon}$, $C_{2\varepsilon}$ – turbulence model constants
$C_{3\varepsilon}$, σ_ε – turbulence model constants
d – injector diameter
D_α – mixture diffusion coefficient, [m^{2}s^{-1}]
h_α – enthalpy of a c
L – chamber length, [m]
P – static pressure, [Pa]
r – radial position, [m]
R – universal gas constant, [Jmol^{-1}K^{-1}]
S_{ij} – rate of strain tensor
T – static temperature, [K]
u – velocity, [ms^{-1}]
V – volume, [m^3]
Y_α – mass fraction of a component α
x – Cartesian co-ordinate, [m]
X – axial chamber position, [m]

Greek symbols

λ – thermal conductivity, [Wm^{-1}K^{-1}]
ρ – density, [kgm^{-3}]
υ – molar volume, [m3mol–1]
ω_{ij} – rotation tensor

Super and sub-scripts

$\bar{}$ – Reynolds averaging
$''$ – fluctuation
$\sim$ – Favre averaging
c – centreline value
0 – centreline value at the injector outlet
∞ –chamber property away from the jet
+ – dimensionless value
ch – chamber
inj – injector
inlet – injector inlet

References

[1] Lu, F. K., Braun, E. M., Rotating Detonation Wave propulsion: Experimental Challenges Modelling, and Engine Concepts, *Journal of Propulsion and Power*, *30* (2014), 5, pp. 1125-1142
[2] Haidn, J., Habiballah, M., Research on High Pressure, Cryogenic Combustion, *Aerospace Science and Technology*, *7* (2003), 6, pp. 473-491
[3] Gomet, L., *et al*., Lagrangian Modelling of Turbulent Spray Combustion under Liquid Rocket Engine Conditions, *Acta Astronautica*, *91* (2014) 1, pp. 184-197
[4] Vigneshwaran, S., *et al*., Wall Heat Flux Mapping of Liquid Rocket Thrust Chamber with Multi-Attitude GH_2/GO_2 Jets, *Proceedings*, 53rd AIAA/SAE/ASEE Joint Propulsion Conference, Atlanta, Geo., USA, 4766, 2017
[5] Candel, S., *et al*., Advances in Combustion and Propulsion Applications, *European Journal of Mechanics B/Fluids*, *40* (2003), July-Aug., pp. 87-106
[6] Oschwald, M., *et al*., Injection of Fluids into Supercritical Environments, *Combustion Science and Technology*, *178* (2006), 1-3, pp. 49-100
[7] Jarczyk, M., Pfitzner, M., Large Eddy Simulation of Supercritical Nitrogen Jets, *Proceedings*, 50th AIAA Aerospace Sciences Meeting Including the New Horizons Forum and Aerospace Exposition, Nashville, Tenn., USA, 2012, p. 1270
[8] Mayer W., Kruelle, G., Rocket Engine Coaxial Injector Liquid/Gas Interface Flow Phenomena, *Journal of Propulsion and. Power*, *11* (1995), 3, pp. 513-518
[9] Mayer, W., Tamura, H., Propellant Injection in a Liquid Oxygen/Gaseous Hydrogen Rocket Engine, *Journal of Propulsion and Power*, *12* (1996), 6, pp. 1137-1147
[10] Smith, J., *et al*., Supercritical LOX/Hydrogen Rocket Combustion Investigations Using Optical Diagnostics, *Proceedings*, 38th AIAA/ASME/SAE/ASEE Joint Propulsion Conference & Exhibit, Indianopolis, Ind., USA, 2002, p. 4033

[11] Candel, S., *et al*., Experimental Investigation of Shear Coaxial Cryogenic Jet Flames, *Journal of Propulsion and Power*, *14* (1998), 5, pp. 826-834
[12] Mayer, W., Raman Measurements of Cryogenic Injection at Supercritical Pressure, *Heat and Mass Transfer*, *39* (2003), July, pp. 709-719
[13] Chehroudi, B., Raman Scattering Measurements in the Initial Region of Sub- and Supercritical Jets, *Proceedings*, 36th AIAA/ASME/SAE/ASEE Joint Propulsion Conference and Exhibit, Huntsville, Ala., USA, 2000, p. 3392
[14] Oschwald, M., Schik, A., Supercritical Nitrogen Free Jet Investigated by Spontaneous Raman Scattering, *Experiments in Fluids*, *27* (1999), Nov., pp. 497-506
[15] Branam, R., Mayer, W., Characterization of Cryogenic Injection at Supercritical Pressure, *Journal of Propulsion and Power*, *19* (2003), 3, pp. 342-355
[16] Oefelein, J. C., Mixing and Combustion of Cryogenic Oxygen-Hydrogen Shear-Coaxial Jet Flames at Supercritical Pressure, *Combustion Science and Technology*, *17*8 (2006), 1-3, pp. 229-252
[17] Hosangadi, A., *et al*., The 3-D Hybrid RANS/LES Simulations of a Supercritical Liquid Nitrogen Jet, *Proceedings*, 44th AIAA/ASME/SAE/ASEE Joint Propulsion Conference & Exhibit, Hartford, Conn., USA, 2008, p. 5227
[18] Schmitt, T., *et al*., Large-Eddy Simulation of transcritical flows, *C. R. Mecanique*, *337* (2009), 6-7, pp. 528-538
[19] Cheng, G. C., Farmer, R., Real Fluid Modelling of Multi-Phase Flows in Liquid Rocket Engine Combustors, *Journal of Propulsion and Power*, *22* (2006), 6, pp. 1373-1381
[20] Poschner, M., Pfitzner, M., Real gas CFD simulation of supercritical H_2-LOX combustion in the Mascotte Single-Injector Combustor Using a Commercial CFD Code, *Proceedings*, 46th AIAA Aerospace Sciences Meeting and Exhibit, Reno, Nev., USA, 2006, p. 952
[21] Kim, T., *et al*., Numerical Analysis of Gaseous Hydrogen/Liquid Oxygen Flamelet at Supercritical Pressures, *International Journal of Hydrogen Energy*, *36* (2011), 10, pp. 6303-6316
[22] Riahi, Z., *et al*., Numerical Study of Turbulent Normal Diffusion Flame CH_4-AIR Stabilized by Coaxial Burner, *Thermal Science*, *17* (2013), 4, pp. 1207-1219
[23] Benmansour, A., *et al*., A 3-D Numerical Study of LO_2/GH_2 Supercritical Combustion in the ONERA Mascotte Test-Rig Configuration, *Journal of Thermal Science*, *25* (2016), 1, pp. 97-108
[24] Benarous, A., Liazid, A., H_2-O_2 Supercritical Combustion Modelling Using a CFD Code, *Thermal Science*, *13* (2009), 3, pp. 139-152
[25] Kim, T., *et al*., Real-Fluid Flamelet Modelling for Gaseous Hydrogen/Cryogenic Liquid Oxygen Jet Flames at Supercritical Pressure, *Journal of Supercritical Fluids*, *58* (2011), 2, pp. 254-262
[26] De Giorgi, M., *et al.*, Application and Comparison of Different Combustion Models of High Pressure LOX/CH_4 Jet Flames, *Energies*, *7* (2014), 1, pp. 477-497
[27] Kim, S. K., *et al*., Thermodynamic Modelling Based on a Generalized Cubic Equation of State for Kerosene/LOx Rocket Combustion, *Combustion and Flame*, *159* (2012), 3, pp. 1351-1365
[28] Müller, H., *et al*., Large-Eddy Simulation of Nitrogen Injection at Trans- and Supercritical Conditions, *Physics of Fluids*, *28* (2016), 015102
[29] Soave, G., Equilibrium Constants from a Modified Redlich-Kwong Equation of State, *Chemical Engineering Science*, *27* (1972), 6, pp. 1197-1203
[30] Peng, D. Y., Robinson, D. B., A New Two-Constant Equation of State, *Industrial and Engineering Chemistry Fundamentals*, *15* (1976), 1, pp. 59-64
[31] Aungier, R. H., A Fast, Accurate Real Gas Equation of State for Fluid Dynamic Analysis Applications, *Journal of Fluids Engineering*, *117* (1995), 2, pp. 277-281
[32] Launder, B. E., *et al*., Prediction of Free Shear Flows – A Comparison of Six Turbulence Model, NASA Langley Res. Center Free Turbulent Shear Flows, USA, 1973, Vol.1, pp. 361-426
[33] Cheng, G. C., Farmer, R., Development of Efficient Real-Fluid Model in Simulating Liquid Rocket Injector Flows, *Proceedings*, 39th AIAA/ASME/SAE/ASEE Joint Propulsion Conference and Exhibit, Huntsville, Ala., USA, 2003, p. 4466
[34] Pope, S. B., An Explanation of the Turbulent Round-jet/plane-jet Anomaly, *AIAA Journal*, *16* (1978), 3, pp. 279-281
[35] Harsha, P. T., *Free Turbulent Mixing: A Critical Evaluation of Theory and Experiment*, Turbulent Shear Flows, CP-93, AGARD, 1971
[36] Chehroudi, B., *et al*., Initial Growth Rate and Visual Characteristics of a Round Jet into a Sub- to Supercritical Environment of Relevance to Rocket, Gas Turbine, and Diesel Engines, *Proceedings*, 37th Aerospace Sciences Meeting and Exhibit, Reno, Nev., USA, 1999. p. 206

[37] Bensalem, C., *et al*., Vers la caractérisation du mélange en sortie d'un injecteur coaxial cryotechnique: Influence de la loi de comportement (Towards the characterization of the mixture at the output of a cryogenic coaxial injector: Influence of the law of behavior – in French), *Proceedings*, 23th Congrès Français de Mécanique, Lille, France, 2017, S11, 130196
[38] Haidn, O. J., Atomization, Combustion, and Heat Transfer, Second International Workshop on Rocket Combustion Modelling, Lampoldshausen, Germany, 2001
[39] ***, ANSYS FLUENT v16.2, Inc., Canon-sburg, PA, USA, 2016
[40] Cheng, G. C., Farmer, R., The CFD Simulation of Liquid Engine Rocket Injectors Part 1, Simulations of the RCM-1 Experiments, *Proceedings*, 2nd International Workshop on Rocket Combustion Modelling, Lampoldshausen, Germany, 2001
[41] Banuti, D. T., Hannemann, K., The Absence of a Dense Potential Core in Supercritical Injection: A Thermal Break-up Mechanism, *Physics of Fluids*, *28* (2016), 035103

Paper submitted: August 5, 2019
Paper revised: February 27, 2020
Paper accepted: March 27, 2020